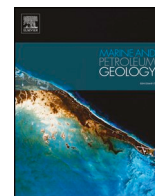




ELSEVIER

Contents lists available at ScienceDirect

Marine and Petroleum Geology

journal homepage: www.elsevier.com/locate/marpetgeo

Research paper

Potential freshening impacts on fines migration and pore-throat clogging during gas hydrate production: 2-D micromodel study with Diatomaceous UBGH2 sediments

Junbong Jang^{a,2}, Shuang C. Cao^{b,1}, Laura A. Stern^c, William F. Waite^d, Jongwon Jung^{e,*}, Joo Yong Lee^f

^a Integrated Statistics, Inc., Contracted to U. S. Geological Survey, Woods Hole, MA, USA

^b Fugro USA Marine, Inc., Houston, TX, USA

^c U. S. Geological Survey, Menlo Park, CA, USA

^d U. S. Geological Survey, Woods Hole, MA, USA

^e School of Civil Engineering, Chungbuk National University, Cheongju, Chungbuk, South Korea

^f Petroleum and Marine Research Division, Korea Institute of Geoscience and Mineral Resources, Daejeon, South Korea

ARTICLE INFO

Keywords:

Gas hydrate
Ulleung basin
Fines migration
Freshening
Micromodel
Sedimentation test

ABSTRACT

The methane gas hydrate stored in natural sediments is considered a potential gas resource. Countries such as China, India, Japan, and Korea are interested in commercializing this resource, and offshore field pilot tests for gas production have been conducted using depressurization methods to destabilize gas hydrate and facilitate the migration of methane to the production well. However, fine-grained sediments (fines), which are present even in coarse-grained, gas hydrate-bearing sediments, can be resuspended in the production fluid, subsequently clogging pore throats in the formation and reducing the overall production efficiency. We conducted laboratory tests to evaluate the suspension and clogging potential of fines collected from the Ulleung Basin, East Sea, Korea during the 2010 Ulleung Basin Gas Hydrate Expedition 2 (UBGH2). Experimental results reveal that diatoms are prevalent in the sediment and largely control the suspension and clogging behavior. Fluid flow experiments in 2D micromodels show clogging occurs even when injecting the minimum sediment concentration (0.1 wt% in the fluid) through micromodels with pore-throat widths at the high end of the anticipated range for UBGH2 gas hydrate-bearing sands (100 μm). Mobile gas/fluid interfaces forming during gas hydrate dissociation accentuate clogging by concentrating and mobilizing fines. Sedimentation tests show pore-water freshening during dissociation is not anticipated to change the potential for diatoms to become entrained in the pore water flow, even for the observed gas hydrate saturations of $\sim 80\%$. Muscovite and illite are also significant components of the tested sediment, however, and pore-water freshening increases their potential for resuspension and clogging. Overall, the resuspension and clogging potential of these fine sediments should increase as gas hydrate dissociation progresses in the thin, gas hydrate-bearing sands investigated in the Ulleung Basin.

1. Introduction

Highly concentrated methane can be found in naturally-occurring gas hydrate, a crystalline solid that can be found in permafrost environments and deep-water marine sediments and other locations where the gas hydrate stability requirements of elevated pressure and low temperatures are met (Collett et al., 2009; Sloan and Koh, 2007). Among these natural occurrences, gas hydrate hosted in the existing

pore space of sand is thought to be the most promising gas hydrate occurrence type for economic energy resource production (Boswell and Collett, 2011; Boswell et al., 2014).

Currently, depressurization is considered the most economical method for destabilizing gas hydrate and extracting methane from gas hydrate bearing sediments (Boswell et al., 2014), but geomechanical consequences of depressurization must be accounted for to optimize the overall methane extraction. One challenging consequence of

* Corresponding author.

E-mail address: jjung@chungbuk.ac.kr (J. Jung).

¹ Formerly Civil and Environmental Engineering, Louisiana State University, Baton Rouge, LA, USA.

² Currently Department of Civil Engineering, Dong-A University, Busan, South Korea.

depressurization is sediment mobilization, which occurs in response to the induced fluid flow and evolving effective stress state. Ongoing and recent production testing onshore in the United States (Anderson et al., 2014; Boswell et al., 2019a) and Canada (Dallimore and Collett, 2005; Kurihara et al., 2011), as well as offshore Japan (Yamamoto et al., 2014, 2019) and China (Li et al., 2018), demonstrates that methane extraction from naturally-occurring gas hydrate reservoirs is feasible, but reinforces the importance of understanding and controlling sediment mobilization (Anderson et al., 2014; Li et al., 2018; Yu et al., 2019). Sediment mobilization and migration along permeable layers toward or into the production well not only reduce well productivity, but have also caused production tests to terminate prematurely (e.g. Dallimore et al., 2012; Yamamoto et al., 2017).

The fluid flow rates required to mobilize sand-sized grains are an order of magnitude higher than those required to mobilize fine-grained particles (particle diameters $< 75 \mu\text{m}$ (ASTM D2487-11, 2011)) (Oyama et al., 2016). Even if sand controls are utilized, production activities can mobilize fines present within the gas hydrate reservoir. As noted by Hancock et al. (2019), in thinly-layered gas hydrate reservoirs, fines migration must be carefully considered during production because, once mobilized, fine-grained particles can collect in pore throats, clogging production flow paths, reducing the reservoir permeability (i.e., reservoir formation damage) and overall production efficiency (Cao et al., 2019; Jung et al., 2012; Oyama et al., 2016; Valdes and Santamarina, 2007).

This work analyzes the clogging potential of fines associated with deep-water Ulleung Basin gas hydrate reservoirs. Sediment mobility effects are amplified in these deep-water systems (> 2000 m below sea level) because large pressure drawdowns are required for production (Boswell et al., 2019b). Ulleung Basin reservoir production modeling, for example, recommends a pore pressure drawdown of ~ 13 MPa (Kim et al., 2018; Moridis et al., 2013, 2019). Moreover, coring during the 2010 Ulleung Basin Gas Hydrate expedition 2 (UBGH2) revealed gas hydrate-bearing sands existing as thin (< 1 m) layers interbedded with fine-grained sediment (Bahk et al., 2013; Ryu et al., 2013). Because the hydrate-bearing sands are thin, the pressure drawdown cannot be applied to the individual sand layers alone and must instead be applied to the full interval of alternating sand and fine-grain layers (Kim et al., 2018; Moridis et al., 2013, 2019).

Gas hydrate dissociation, which is endothermic (Handa, 1986), is most active at the interfaces between gas hydrate bearing sands and neighboring fine-grained interbeds because of the latent heat available in the fine-grained interbeds (Moridis et al., 2019; Myshakin et al., 2019; Yamamoto et al., 2017). Preferential gas hydrate dissociation at the sand/fine-grained sediment interfaces not only dramatically increases the likelihood of sand mobilization and migration toward the production well (Uchida et al., 2019), but also promotes erosion of the fine-grained layer. This increases the concentration of mobilized fines in the production fluid (Oyama et al., 2016), thereby increasing the potential for fines to migrate into the coarser-grained layer where they can reduce production efficiency by clogging pore throats.

Conceptually, pore-throat clogging can be viewed as a mechanical process in which the clogging mechanism is controlled by the relative sizes of the mobilized particle and the pore throat (Fig. 1; Bigno et al., 1994; Oyenein et al., 1995; Khilar and Fogler, 1998; Dressaire and Sauret, 2017). As summarized by Cao et al. (2019), when particle sizes are 1% or less of the pore-throat opening, particles can pass without clogging. As particle sizes rise to $\sim 10\%$ of the pore-throat opening, multiparticle blockages can form, and as the particle sizes increase, these blockages or bridges can be formed with fewer and fewer particles until individual particles themselves are too large to pass through the pore throats (i.e. sieving).

Due to their small size, fine-grained particles could be anticipated to individually pass pore throats without clogging (Fig. 1a). Due to their small mass and relatively large surface charge densities, however, fines are prone to electrical interactions that promote not only the

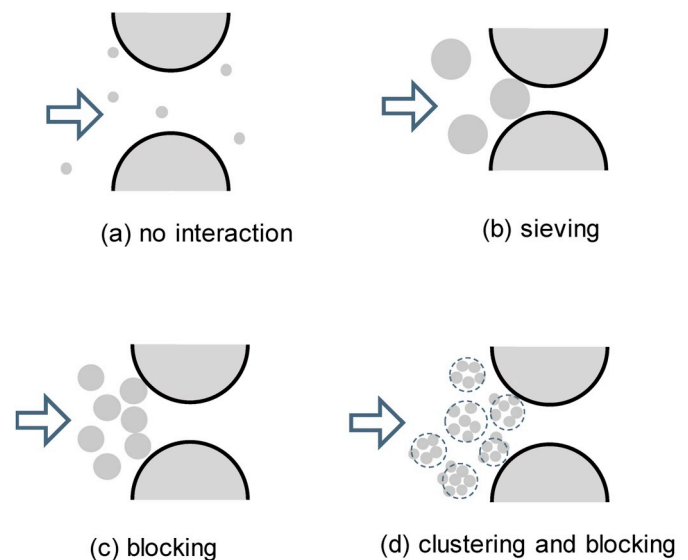


Fig. 1. Fines migration and physical clogging types at a pore throat (modified from Cao et al., 2019): (a) no interaction, (b) clogging as sieving, (c) clogging as blocking, (d) clogging as clustering and blocking – pore fluid chemistry and grain compositions affect the clustering.

detachment of fines from the sediment fabric, i.e. resuspension (Civan, 2016; Jang et al., 2018a), but also the subsequent clustering of fines in the pore fluid (Lambe and Whitman, 1969; Mitchell and Soga, 2005; Jang et al., 2018a). Clustering effectively increases the size of a fine grained “particle,” increasing the likelihood of clogging (Fig. 1d). The nature of the electrical interactions depends on several parameters, including the fines’ mineralogy, the pore water chemistry (particularly the pore-water salinity), and the presence or absence of a mobile gas water interface (Muecke, 1979; Ivanov et al., 1986; Jung et al., 2012; Han et al., 2018).

These parameters are particularly relevant during gas hydrate production activities because gas hydrate dissociation liberates pure water and free methane gas, thereby reducing the pore-water salinity and creating mobile gas/water interfaces. How the fines’ behavior evolves in this dynamic environment depends on the fines’ mineralogy as well as particle morphology.

In this study, 2D micromodel and sediment characterization of fine-grained sediments from two gas hydrate reservoir sites in the Ulleung Basin, recovered during UBGH2, are combined to provide insight into the expected behavior of fines during depressurization-induced production. 2D micromodel tests examine clogging behavior of fines as a function of fines concentration, pore-water salinity and gas/water interface migration. Sedimentation tests, in which fines are observed as they settle in fluids of different pore chemistry, provide additional insight into the resuspension and clustering behavior of the UBGH2 fines. Optical microscope and scanning-electron microscope (SEM) observation, analysis of mineralogy and tests of Atterberg limits are used to characterize the UBGH2 fines and aid in interpreting the micromodel and sedimentation test results.

2. Geological setting in Ulleung Basin for UBGH2

The Ulleung Basin’s geologic history provides insight not only into the distribution of sediment available to host gas hydrate, but also into the fluid flow mechanisms thought to be responsible for supplying methane-rich fluids to those reservoir-quality sediments. The Ulleung Basin is a back-arc basin formed during seafloor spreading and subsidence beginning in the Late Oligocene (Chough and Barg, 1987). The Japanese islands initially moved away from the Eurasian continent as the basin grew. In the Late Miocene, plate-motion shifts caused the

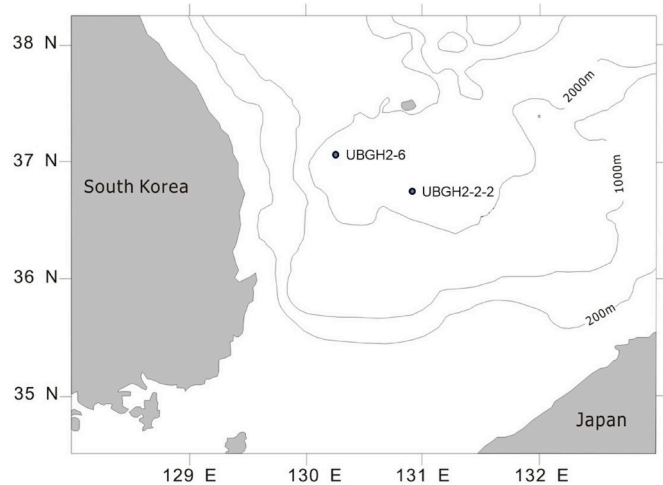


Fig. 2. UBGH2 sites in this study (after Lee et al., 2013a,b): Both sites target gas hydrate in alternating layers of turbidite sands and fine-grained hemipelagic sediment. At UBGH2-6 these layers are bounded by a normal fault that may supply methane to the turbidite sands (Ryu et al., 2009; Yoo et al., 2013). At UBGH2-2-2 these layers are adjacent to a chimney investigated in UBGH1 and offer a chance to observe the extent of gas hydrate beyond the bounds of the chimney (Bahk et al., 2013).

Japanese islands to begin moving back toward the mainland (Chough and Barg, 1987; Lee and Suk, 1998), imposing compressional deformation on the Ulleung Basin that continues to the present day (Ingle, 1992). The ongoing closure has important consequences for sediment deposition and fluid flow in the basin.

The back-arc closure was accompanied by uplift, particularly in the southern portion of the basin (Bahk et al., 2013; Ingle, 1992), and this in turn triggered slope failures that created a basin-wide distribution of mass transport deposits in the Late Miocene and Pliocene (Lee and Suk, 1998). As the deformation rate slowed in the Pleistocene and Holocene, mass transport deposits were restricted to the more steeply-sloped southern portion of the basin. The sites considered here, UBGH2-2-2 and UBGH2-6, are located near the center and northwest of the deepest portion of the Ulleung Basin, respectively (Fig. 2). This area has experienced alternating turbidite and hemipelagic sedimentation (Lee and Suk, 1998). The predominantly coarse-grained turbidite sands represent the primary coarse-grained gas hydrate reservoir sediment in the Ulleung Basin (Bahk et al., 2013), and the interbedded fine-grained hemipelagic sediments are gas hydrate-free beds within the layered gas hydrate reservoir.

In addition to influencing the distribution of coarse and fine-grained sediment in Ulleung Basin, the back-arc closure also deformed and

compressed the sediment (Chough and Barg, 1987). Sediment deformation, along with rapid sedimentation (Kim et al., 2013), also generated excess pore pressure that created fracture-based chimney structures near UBGH2-2-2 (Ryu et al., 2013; Yoo et al., 2013) and likely drove the vertical migration of methane-rich fluids thought to be responsible for the sourcing the observed gas hydrate occurrences (Kim et al., 2011; Ryu et al., 2009). Based on findings from an earlier expedition (UBGH1, in 2007) of gas hydrate within a chimney structure at Site UBGH1-9 (Kim et al., 2011), Site UBGH2-2-2 targeted the high seismic-amplitude, flat-lying turbidite and hemipelagic sediment adjacent to UBGH1-9 to investigate the degree to which gas hydrate extends beyond the bounds of the UBGH1-9 chimney (Bahk et al., 2013).

Sediment compression in the Ulleung Basin also triggered faulting in the vicinity of UBGH2-6 (Yoo et al., 2013). Site UBGH2-6 was chosen to test flat-lying turbidite and hemipelagic layers with relatively strong seismic reflections that terminate at the adjacent normal fault (Lee and Collett, 2013; Yoo et al., 2013). The fault likely acts as a permeable conduit, delivering methane-rich fluids to the turbidite sands (Ryu et al., 2009; Yoo et al., 2013).

Seismic stratigraphy mapping indicates Pleistocene – Holocene turbidites and hemipelagic sediments overlie the bottom simulating reflector (BSR), and the BSR is near the top of the Pliocene mass transport deposits at both sites (Lee and Suk, 1998; Yoo et al., 2013). This work focuses on turbidite and hemipelagic sediment taken from depths corresponding to the high-amplitude seismic reflections associated with gas hydrate occurrences. Though turbidite sands provide the primary coarse-grained host sediment (d_{50} up to $\sim 134 \mu\text{m}$) for gas hydrate in the Ulleung Basin (Ryu et al., 2013), it is important to note these turbidite sands tend to be thin. At UBGH2-2-2, the turbidite sand thicknesses range from 1 to 14 cm, averaging only 3 cm (Bahk et al., 2013; Ryu et al., 2013). The UBGH2-6 turbidite sand thicknesses are more varied, ranging from 1 to 143 cm, with a 9 cm average.

Because of this thin layering, production via depressurization at either site would involve dissociation along many interfaces between the gas hydrate-bearing, predominantly coarse-grained turbidite sands and adjacent, predominantly fine-grained hemipelagic sediment. This work advances our understanding of the potential for fine-grained interbed sediments from these interfaces to get entrained in the production-induced fluid flow, clog pore throats in the adjacent, coarse-grained gas hydrate-bearing turbidites and consequently reduce permeability and production efficiency.

3. Materials and methods

Three samples, one from Site UBGH2-2-2 and two from UBGH2-6, were selected for this study (Table 1). Based on their grain size, specific surface area and locations within the sediment cores with respect to other lithologies, these samples are inferred to be from the hemipelagic

Table 1
Physical property measurements to the UBGH2 samples.

Type	Location ^a		Depth [mbsf]	Potential hydrate	$d_{90}/d_{60}/d_{50}/$ d_{30}/d_{10} ^b [μm]	G_s ^c []	LL []		PL []	S_s ^d [m^2/g]	dry weight for sedimentation test [g]	
	Hole	Core					Length	LL _{DW}				LL _{2M,corr}
interbed mud	UBGH2-2-2B	15C	45–57 cm	141	hydrate	17.7/7.5/2.9/1	2.664	66	61	–	40	7.49
	UBGH2-6B	18H-3	0–20 cm	135	occurrence zone	16.9/6/4.8/ 2.6/1	2.523	110	92	57	52	3.79
	UBGH2-6C	6P	40–85 cm	178	below BGHSZ	22/8.5/7/3.6/ 1.3	2.499	–	–	43	76	4.49

Remark: “–” No measurement due to lack of material.

^a UBGH2-2-2B: 36° 42' 42.4" N, 130° 53' 42.6" E, Water depth 2093 mbsl; UBGH2-6B: 37° 00' 57.6" N, 130° 16' 00.0" E, Water depth 2153 mbsl; UBGH2-6C: 37° 00' 57.5" N, 130° 15' 59.0" E, Water depth 2153 mbsl.

^b Particle size by a laser-scattering particle analyzer, Microtrac S3500 (Bahk et al., 2013), d_n represents the particle diameter corresponding n percent passing by mass.

^c Specific gravity by gas pycnometer (Pentapycnometer 5200e, Quantachrome Instruments).

^d Specific surface by a wet method using methylene blue solution (Santamarina et al., 2002).

interbed sediments that are layered among the gas hydrate-bearing turbidite sediments (Ryu et al., 2013). The selected samples represent the interfacial fines that can be entrained in coarser-sediments during gas production. The samples were dried for storage after UBGH2 and were resaturated where necessary as described below for certain tests.

Within the framework of understanding how thinly-bedded gas hydrate reservoirs are likely to respond to depressurization-style production techniques, the specific experimental objective of this work is to establish the clogging potential of the UBGH2 test sediments. The 2D micromodel tests provide the primary means of assessing clogging potentials, but as suggested in Fig. 1 (a) and (d), the clogging potential of fines depend on their clustering behavior.

The clustering behavior itself depends on the sediment mineralogy, morphology and pore fluid (Cao et al., 2019; Jang and Santamarina, 2016; Jang et al., 2018a). To provide a comprehensive basis for interpreting the 2D micromodel results and build an understanding of likely sediment responses to production, four types of test were performed in addition to the 2D micromodels. To establish the types of fines present, X-Ray diffraction (XRD) and energy-dispersive X-Ray spectroscopy (EDS) measurements were used. To establish particle morphology, optical and scanning electron microscope (SEM) images were collected. To test how interparticle interaction and clustering behavior depend on pore fluid chemistry, Atterberg limit and sediment tests were performed. Test methods are described below, and Table 1 provides geologic and geotechnical information for the samples used in this study's 2D micromodel and sedimentation experiments.

3.1. Specimen characterization

3.1.1. Microscopic imagery

Particle shapes were captured by a Tescan VEGA-3 variable-pressure scanning electron microscope (SEM). High-vacuum, low-voltage SEM techniques run at room temperature conditions provide high resolution images of the fines. An optical stereo-microscope, Leica DMS1000, shows the overall particle clusters that form when samples are dried.

3.1.2. Mineralogy

Mineral compositions of powdered samples were analyzed by X-ray diffraction (XRD) at the USGS Woods Hole Coastal and Marine Science Center with a Rigaku miniflex 600 benchtop X-ray Diffraction (XRD) unit. The sample was powdered and prepared as described by Poppe et al. (2001). The Rigaku PDXL2 software package was used in the whole powder pattern fitting mode for quantitative analysis of the sample components, and Rietveld method was used for structure refinement. Because diatoms are formed from amorphous silica, however, their XRD response is characterized by a broad, low amplitude hump in the XRD spectra as a function of scanning angle (Fagel et al., 2003; Andrews et al., 2006). This spectral response is not accounted for in the USGS XRD analysis, which is keyed to sharp, high-amplitude responses. After verifying the presence of diatoms in the sediments by SEM, a second set of XRD measurements at KIGAM were conducted using CuK α radiation at 40 kV and 20 mA through a Philips X'pert MPD diffractometer. The XRD analyses were conducted using the software program SIROQUANT that utilized Rietveld quantification methods for improved assessment of diatom contributions to sample mineralogies.

For additional mineralogical insight, Energy-Dispersive X-ray Spectroscopy (EDS) was run during SEM analysis of samples. Because the EDS beam can target specific locations of interest within a given SEM image, the technique can provide semi-quantitative assessment of the elemental makeup of specific grains in each sample.

3.1.3. Atterberg limits: liquid limit (LL) and plastic limit (PL)

The LL and PL are indicators that empirically correlate with physical properties such as permeability, compressibility and shear strength (Wroth and Wood, 1978; Santamarina et al., 2001; Mitchell and Soga, 2005) that are significant for predicting sediment response during long-

term production activities. In this study, liquid limit values were obtained with fall cone tests (British Standard Institute, 1990). Each core sample was tested with deionized water and 2M-brine (2 mol/l salt water) to see how salinity, i.e., ionic concentration, affected the fines behavior. For the samples that did not have enough sediment to divide between both liquid limit tests, a liquid limit test with deionized water (LL_{DW}) was run first, and then the sediment was reused for a liquid limit test with 2M-brine (LL_{2M}). A separate subsample of each core sample was used for a plastic limit test conducted using deionized water and the thread-rolling method (ASTM D4318, 2005).

3.2. Grain-settling-rate-based sedimentation test

The sedimentation test provides insight into how sediment fabric and clustering behavior respond to changes due to pore fluid chemistry changes (Pierre and Ma, 1999; Palomino and Santamarina, 2005; Jang et al., 2018a, b, 2019). The procedures introduced in Jang et al. (2018a, b, 2019) are used in this study and summarized here. First, dried sediment was spooned into a cylindrical mold of 25.4 mm height and diameter. This volume of loose-packed material was weighed, then mixed with added test fluid until the mixture filled 152.4 mm of the sedimentation tube (Fig. 3). The system was allowed to equilibrate for 12 h before the headspace was evacuated to remove gas bubbles and dissolved gas from the sediment pore space. The cylinder was then stoppered, shaken for 60 s, and left undisturbed to settle. The depositional and accumulation interfaces (Fig. 3) were then tracked over time. The selected pore fluids were deionized water, 2M-brine and 0.0654M solution of the sediment dispersant sodium hexa-metaphosphate, (NaPO₃)₆ to see pore-fluid-chemistry effects on sediments.

Since the samples were from marine sediment, dried samples contained salt left behind as the in situ pore water evaporated during the initial sample drying process. Consequently, mixing deionized water with the samples created a pore-water brine of ~0.05M as those salts are re-dissolved. The deionized water mixture is referred to as “deionized water with salt” (DWS). In order to minimize the effects of salt on the fines fabric, the DWS was diluted following the DWS sedimentation test by withdrawing ~60 ml of the clear supernatant from the total mixture volume of 77.2 ml and replacing that ~0.05M brine by deionized water. This solution is referred to as “deionized water (freshened),” (DWF) because the deionized water with salt (DWS) was freshened to ~1–2% of the original salt concentration via this process. A separate split from the original core sample was used for the test in 2M brine. These three distinct fluid salinities provide a means for

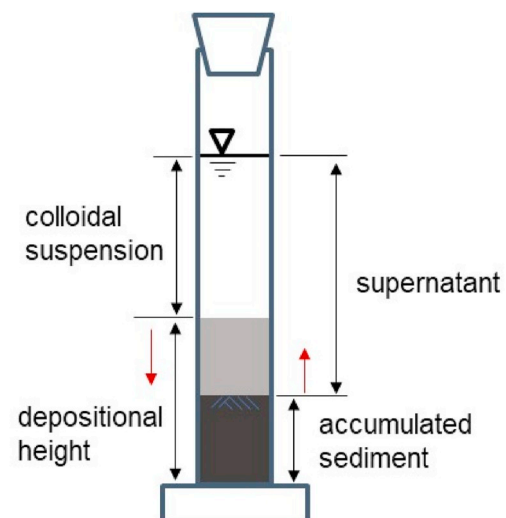


Fig. 3. Sedimentation test configuration and definition of depositional and accumulated interface height for segregated sedimentation.

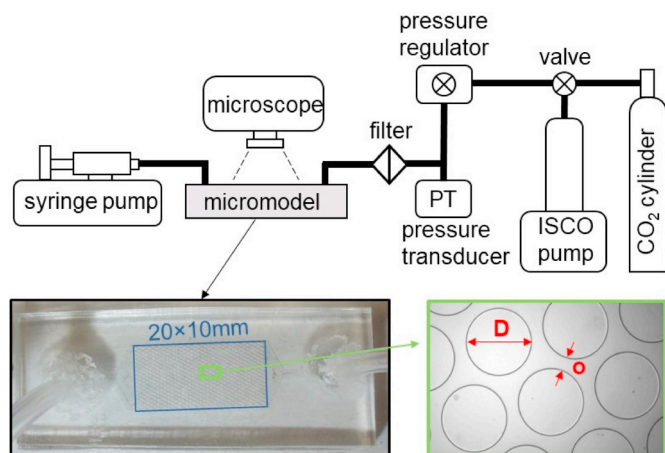


Fig. 4. Experimental configuration of the micromodel apparatus, with a plan view of the 2D micromodel in the lower left image for scale. The 20 × 10 mm rectangle area of the lower-left photo has empty space between the solid cylinders for fluid flow. In the magnified bottom-right photo, the circular shape with the diameter D is a solid cylindrical “grain” and the pore throat (o) is the flow passage.

establishing how sediment clustering behavior changes during the pore-fluid freshening that occurs as gas hydrate dissociates during production. A third split from the original core sample was tested in the dispersant, sodium hexametaphosphate (NaPO_3)₆, an ASTM-recommended fluid for reducing interparticle attraction (ASTM, 2007). The negative ions in (NaPO_3)₆ shield positive ions on the edges of platy particles such as kaolinite, mica and bentonite, preventing platy-particle clustering, and increasing interparticle repulsion (Andreola et al., 2004; Jang et al., 2018a; Lagaly, 1989). Using (NaPO_3)₆ provides insights into the end-member condition of how particles settle in the absence of clustering. The pH of the mixtures was ~ 7 .

3.3. Fluid flow tests in 2D-Micromodel chips

Fig. 4 illustrates the experimental setup (refer to Cao et al., 2018, 2019). The micromodel chip, made of polydimethylsiloxane (PDMS) etched by standard photolithography bonded to a glass slide (McDonald and Whitesides, 2002), has a series of 100 μm -tall cylindrical “grains” with defined gaps, or “pore throats” of the same height. The diameter (D) of the solid cylinder and the pore throat (o) determine the micromodel geometry, with the pore throat being the narrowest geometry for fluid flow. The designed micromodel pore throat widths were 100 μm or less to represent the typical particle size ($\sim 200 \mu\text{m}$) of sandy, gas-hydrate-bearing sediments in the Ullung Basin. The particle size of sandy gas-hydrate bearing sediment is coarser than the sediment that typically prevails in the basin (Bahk et al., 2013).

For each test, the micromodel was placed under a microscope (Olympus IX51-LWD 4X/0.1) and connected to a syringe pump (NE-1010, Kats Scientific) with a liquid mixture (sediment in either deionized water or 2M brine). The opposite edge of the micromodel was connected to an ISCO pump (Teledyne ISCO) filled with CO_2 from an attached CO_2 cylinder (99.99%, Airgas). Prior to injecting the fines mixture, the micromodel was rinsed with ethanol and then pre-saturated with deionized water or 2M-brine.

The concentration of sediment in the liquid mixture was intended to span likely concentrations encountered in natural systems. As observed in natural gas hydrate reservoirs, such as Cascadia Margin, offshore Canada (Torres et al., 2008), Krishna-Godavari Basin, offshore India (Waite et al., 2019) and Nankai Trough, offshore Japan (Santamarina et al., 2015), even predominantly coarse-grained, highly gas hydrate-saturated sands consist of up to 10% clay (particle diameters $< 4 \mu\text{m}$), and this component makes up only a fraction of the total fines content

considered here (particle diameters $< 75 \mu\text{m}$). Based on a simple cubic packing of spherical sand grains, the resuspension of even just a 1% (by weight of sediment) concentration of fines results in a 3% (by weight in fluid) concentration of fines in the pore water, assuming densities of 2.65 g/cm^3 for the sediment, and 1 g/cm^3 for pore water. As fluid moves radially inward toward a production well, the geometric restriction means mobilized sediment concentrations increase as the sediment approaches the well (Valdes and Santamarina, 2007). The lower sediment concentration limit was therefore chosen to be just 0.1% by weight of the fluid, and the upper limit was defined as the concentration for which injected fines were observed to clog pore throats in the micromodel (50 $\mu\text{l}/\text{min}$ injection rate, Reynolds number, $\text{Re} < 1$).

After each injection test, the sediment/fluid mixture was withdrawn from the micromodel at 50 $\mu\text{l}/\text{min}$ by the syringe pump while the pressure regulator and ISCO pump maintained a backpressure of $\sim 10 \text{ kPa}$ with CO_2 gas. This caused a CO_2 gas/water interface to migrate through the micromodel. The microscope and camera were used to acquire imagery during the initial sediment/fluid injection to track how the clogging behavior of fines changed as a function of salinity. During the CO_2 interface migration, the imagery captured how fines were mobilized and concentrated at the interface and subsequently clogged pore throats.

4. Results

4.1. Sample characterization

Table 2 provides the XRD-based, bulk mineralogy for the three Ullung Basin samples used in this study. Muscovite and illite are primary components of these samples. A set of XRD analyses at KIGAM quantified diatom contents (24% in UBGH2-2-15C, 45% in UBGH2-6B-18H-3, 39% in UBGH2-6C-6P), and the microscope and EDS results also indicate that diatoms are prevalent (Fig. 5, Table 3). The sediment tested here is generally too fine to image individual particles optically, but it is apparent from Fig. 5a that the drying process produces hardened aggregated particles, which can be broken down mechanically. Gently-ground samples were used for XRD and SEM. SEM images confirm the presence of diatoms and diatom shards at high concentrations in the UBGH2 samples, a selection of which are shown in Fig. 5b and d, and Fig. 6. Based on SEM-EDS, mineralogy can be inferred for several individual particles based on chemical compositions (Fig. 5c, Table 3). Fig. 5c includes EDS locations to help identify the mineralogy of selected particles. Based on the EDS chemical compositions, the diatoms (e.g. EDS location 155) are confirmed to be silica-based, while platy particles (e.g. EDS locations 156, 158) overlying or neighboring the diatoms are inferred to be clay minerals or mica. Framboidal pyrite, cubic microcrystals of pyrite typically arranged in clusters with raspberry-like morphology, is also commonly observed in the test samples; identification of one cluster was further verified by EDS (Fig. 5c, location 152).

Table 1 provides the bulk physical properties of the samples.

Table 2
Mineralogy based on XRD analysis.

Mineralogy	Sediment sites (content in %)		
	UBGH2-2-2B 15C	UBGH2-6B-18H-3	UBGH2-6C-6P
Quartz	17	15.4	19.5
Muscovite	36.4	10.7	41.8
Illite	1.4	49.2	8
Plagioclase	23	2.8	9.6
Calcite	1.2	13	1.8
Kaolinite	7.2	1.9	0
Dickite	8.1	1.3	11.1
Clinchlore	5.4	5.6	8.2
Total	100	100	100

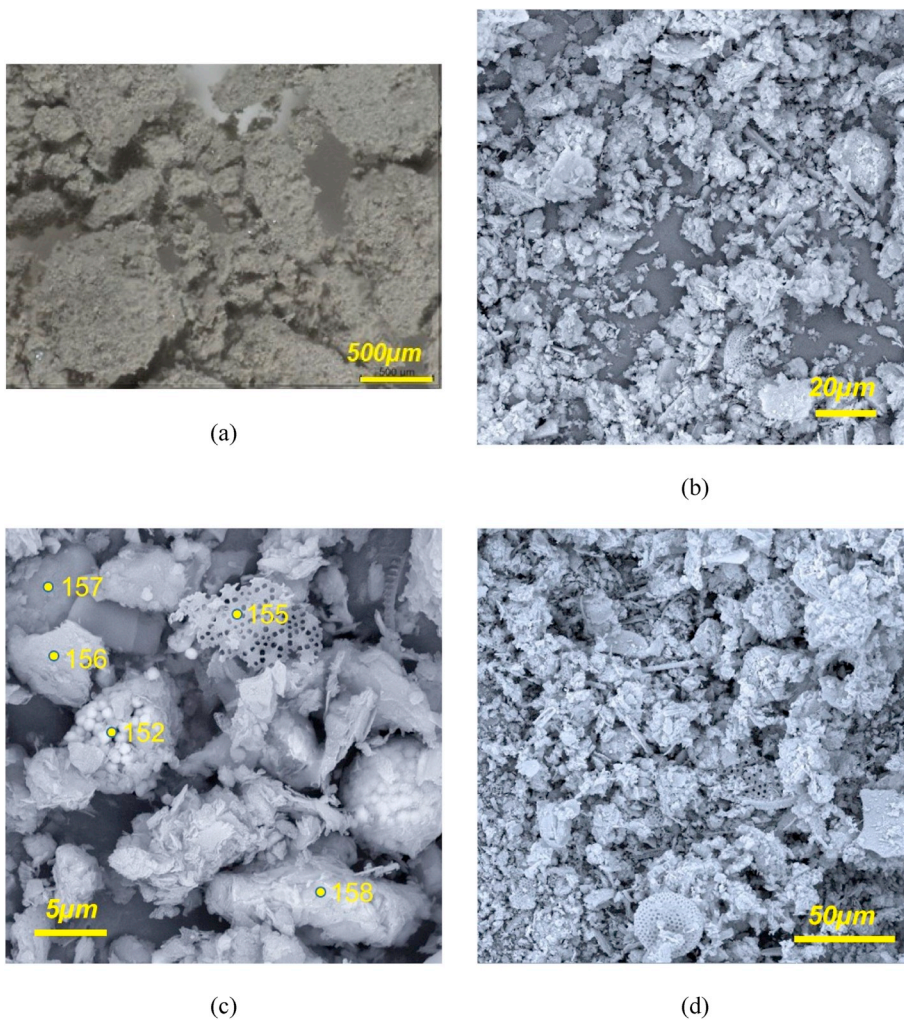


Fig. 5. Microscopic images from the three tested UBGH2 samples. (a) Stereo-microscope image of UBGH2-2-2B-15C showing how the sediment clumps as it dries, which is characteristic of fines; (b) SEM image of UBGH2-2-2B-15C showing the prevalence of diatoms and diatom shards at site UBGH2-2-2, (c) EDS analysis locations for chemical compositions of particles in UBGH2-2-2B-15C (see Table 3), indicating a diatom shard (Location 155), framboidal pyrite (Location 152), and alumino-silicate minerals (Locations 156, 157, 158). (d) SEM image of UBGH2-6B-18H-3, showing the prevalence of diatoms and diatom shards at site UBGH2-6. Expanded views of diatoms from all three samples are shown in Fig. 5.

Table 3
Elemental content based on EDS spectra (see Fig. 5c for locations). Compositions are semi-quantitative and may include signals from adjacent or underlying grains. The processing option used here is oxygen by stoichiometry (normalized): the element content is semi-quantitative and normalized by estimated oxygen quantity.

Element	Spectral Location (Content in %)				
	152	155	156	157	158
O	48.4	47.2	42.8	45.2	47.4
Si	2.0	30.7	19.5	23.5	30.6
Fe	21.8	4.6	15.0	4.6	5.6
S	25.9	0.0	0.0	0.0	0.0
Al	0.8	9.8	12.3	14.7	8.8
Na	0.3	2.4	0.6	0.7	0.5
Cl	0.0	2.0	0.0	0.0	0.0
K	0.3	1.6	1.6	7.1	2.5
Mg	0.0	1.0	6.2	2.2	2.4
Ca	0.3	0.8	1.4	1.1	0.6
Ti	0.2	0.0	0.0	0.7	0.4
Mn	0.1	0.0	0.6	0.3	1.3

Previous geotechnical property measurements such as compressibility, Atterberg limits and specific surface on UBGH1 and UBGH2 samples noted the effects of diatoms on measured properties (Lee et al., 2013a,b; Kwon et al., 2011), and the effects of diatoms on the physical properties are recognizable in these samples as well. Both illite (Specific gravity, $G_s = \sim 2.71$) and muscovite ($G_s = \sim 2.82$) are abundant, but the

presence of diatoms ($G_s = \sim 2.23$) results in a lower specific gravity overall than illite and muscovite would produce. Specific surface, PL and LL are influenced by not only platy particles such as muscovite and illite, but also by diatoms, which have internal porosity (Tanaka and Locat, 1999; Shiwakoti et al., 2002; see also Fig. 6). The diatom content (24% in UBGH2-2-15C, 45% in UBGH2-6B-18H-3, 39% in UBGH2-6C-6P) correlates with the specific gravity, Atterberg limits, and specific surface values in Table 1. However, the ratio of LL_{DW} to $LL_{2M,corr}$ (the liquid limit corrected for the salt weight) of UBGH2-2-2B-15C is 1.08. This value is lower than the 1.20 measured for UBGH2-6B-18H-3 even though both samples are rich in diatoms, which are characterized by a ratio of 1.07 (Jang et al., 2018a). This may be due to other mineral components in the samples: UBGH2-2-2B-15C contains higher fractions of minerals such as quartz and plagioclase while UBGH2-6B-18H has more illite. Consequently, LL is little-changed in UBGH2-2-2B-15C, driving down the $LL_{DW}/LL_{2M,corr}$ ratio relative to what is observed for UBGH2-6B-18H-3 (Table 2).

4.2. Grain-settling-rate-based sedimentation test

Sedimentation tests with the UBGH2 samples show segregation behavior, meaning particles are responding to two governing processes: the sedimentation of larger particles or clusters is controlled primarily by gravity, and forms the accumulated interface at the bottom of the sedimentation tube (Figs. 3a and 5); the sedimentation of smaller particles is more significantly influenced by electrical interparticle forces, and forms the falling depositional interface (Figs. 3a and 5). The

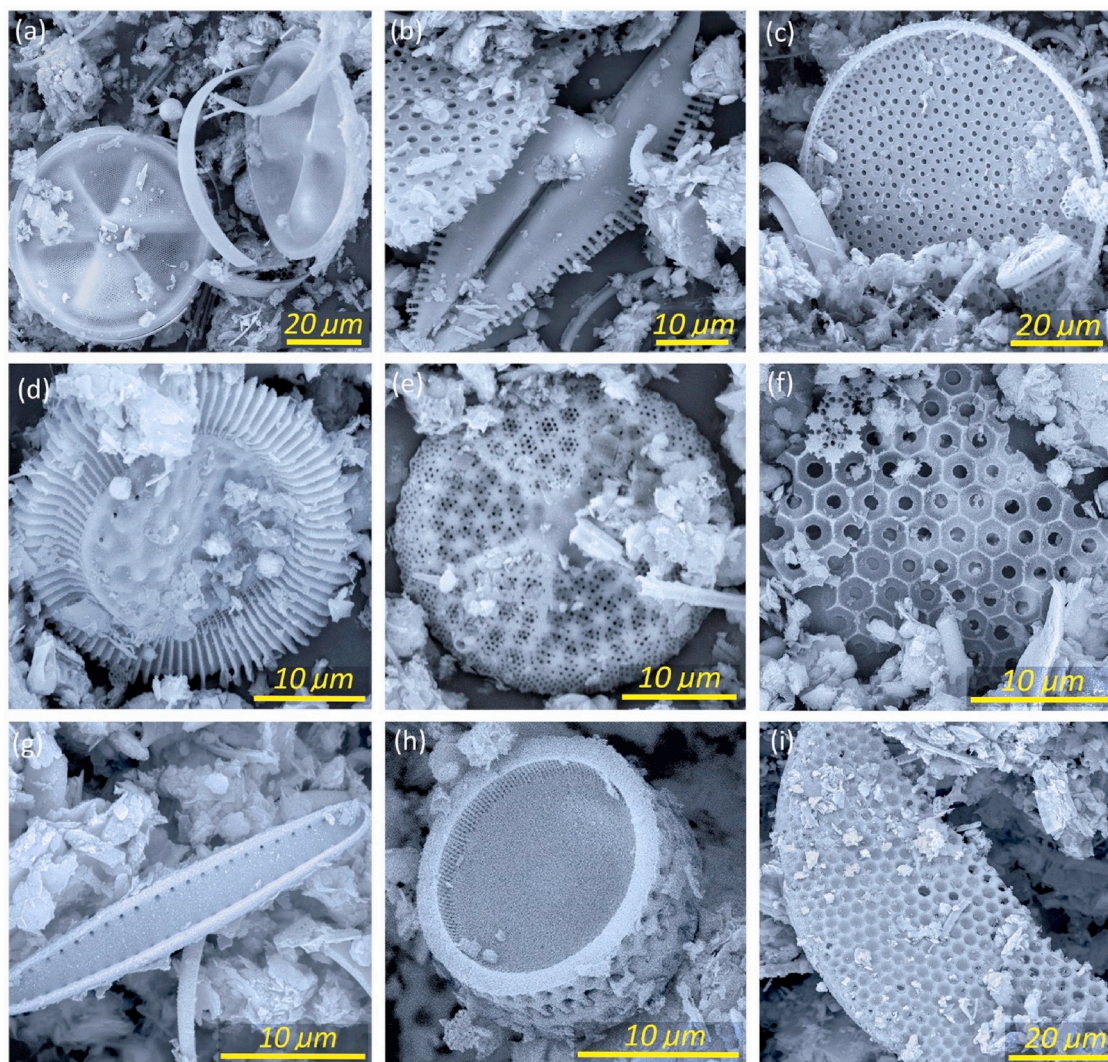


Fig. 6. SEM Images showing the variety of morphologies, sizes, patterning, and nano-to micro-scale porosity of diatoms and diatom shards from UBGH2-6C-6P (panels a–e), UBGH2-2-2B-15C (panel f) and UBGH2-6B-18H-3 (panels g–i).

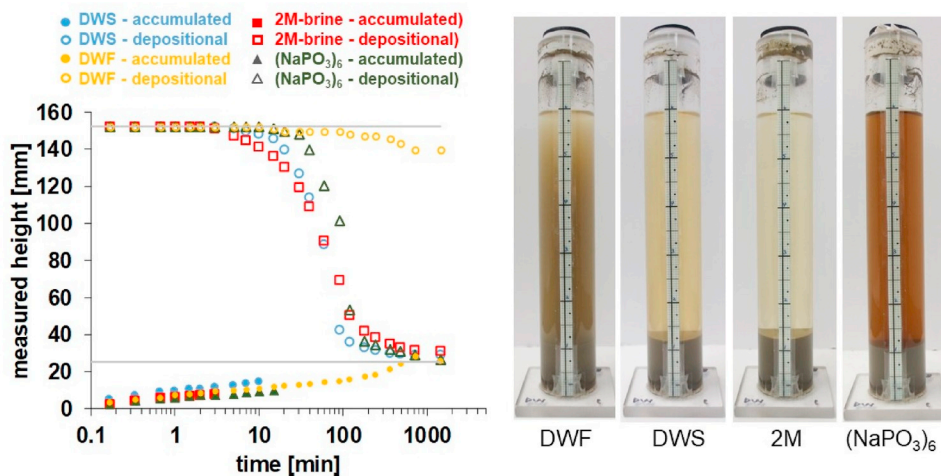
depositional interface indicates the transition between the cloudy fluid in which particles are still suspended and the overlying clear supernatant from which all fines have already settled.

Fig. 7 shows the interface height changes during segregated sedimentation of three samples. The sedimentation behavior is similar for all three samples, most notably showing a decreasing depositional interface height that illustrates how the presence of pore-water ions in the brine allows particles to cluster and settle more rapidly. In comparison, the freshened pore water and dispersant results show particles are remaining in suspension and not clustering. Results for the $(\text{NaPO}_3)_6$ solution test of UBGH2-2-2B-15C do not follow this trend, but this is likely an artifact of having too little sample material for separate sedimentation tests. For UBGH2-2-2B-15C, the $(\text{NaPO}_3)_6$ solution test was conducted by reusing the saturated sample after the 2M-brine test. Despite replacing the clear supernatant above the accumulated interface after the 2M brine test with $(\text{NaPO}_3)_6$ solution, the pore water salinity would allow sedimentation to be controlled more by attractive interparticle forces that promote clustering due to ions in the pore water than by the dispersive, repulsive interparticle forces imposed by the adsorption of $(\text{NaPO}_3)_6$ ions on the particle surfaces.

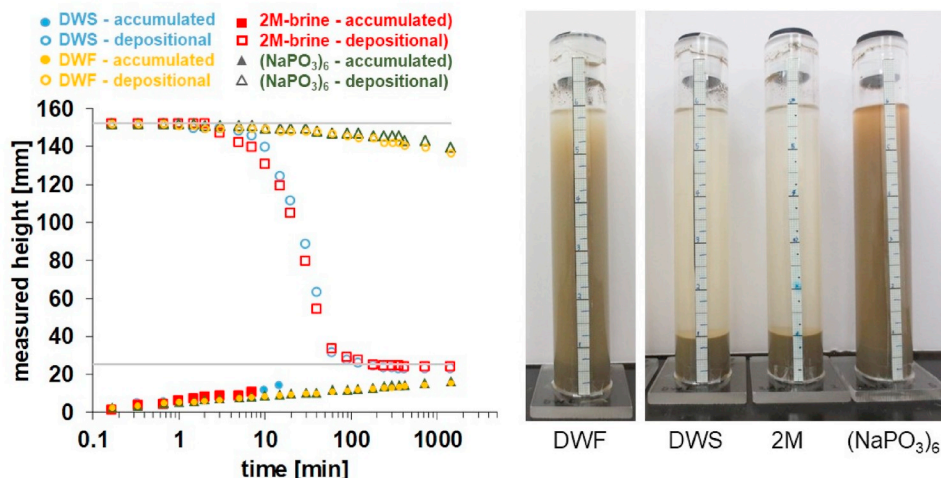
The dependence of sedimentation and supernatant turbidity on pore water salinity can be understood in terms of the Sogami-Ise model (Sogami and Ise, 1984). Negatively-charged particles are attracted to positive pore-water ions (Na^+) in the brine, and, where Na^+ ions

collect between suspended particles, the particles can move closer together and begin to cluster and settle. In Fig. 6, the DWS results are quite similar to the 2M brine results, even though the DWS salinity comes only from dissolving the sediment's salt. The diluted salt concentration is only $\sim 8\%$ of the in situ salt concentration based on the residual weight of the clear supernatant after drying. After the DWS testing, the supernatant is replaced by deionized water for the deionized water (freshened) DWF test, and this dilution to $\sim 1\text{--}2\%$ of the in situ salinity may reduce ionic concentration enough to hamper particle clustering (refer to Sogami-Ise model). Consequently, the sedimentation slows dramatically, and fine particles remain suspended in a turbid supernatant even at the end of the test. The supernatants in the $(\text{NaPO}_3)_6$ solutions for UBGH2-6B-18H-3 and UBGH2-6C-6P were also turbid. Unlike the salt solution ions, however, ions in the dispersant $(\text{NaPO}_3)_6$ solution adhere and cover particles, accentuating the Coulombic like-charge repulsion between particles, which hinders clustering and settlement (Lagaly, 1989; Andreola et al., 2004).

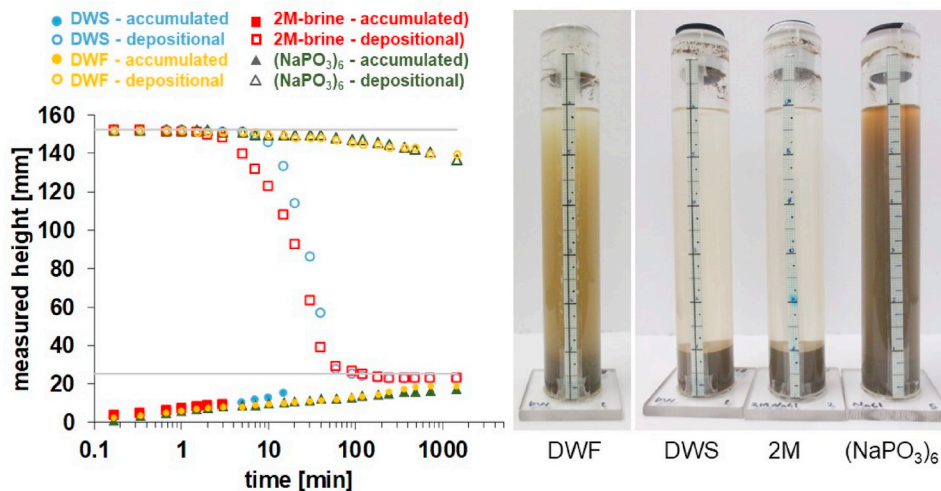
When the supernatant contains fines and is turbid, the final heights of the accumulated interface are less than 25.4 mm, as illustrated in the DWF and $(\text{NaPO}_3)_6$ test results. This is because some sediment remains suspended and cannot contribute to the accumulated sediment height. In contrast, the final accumulated interface heights in DWS and 2M-brine, which have clear supernatants, are close to 25.4 mm. All of the original sediment settles and can contribute to the accumulated



(a) UBGH2-2-2B-15C



(b) UBGH2-6B-18H-3



(c) UBGH2-6C-6P

Fig. 7. Sedimentation tests with UBGH2 samples in deionized water with salt (DWS), diluted DWS (DWF), 2M brine (2M) and $(\text{NaPO}_3)_6$ solution. Horizontal reference lines represent 152.4 mm, the fluid column height, and 25.4 mm, the initial height of each dry, loose-packed specimen. Measured heights of (a) UBGH2-2B-15C, (b) UBGH2-6B-18H-3, (c) UBGH2-6C-6P; The photos show the final interface status 24hr after the beginning of the test. In all cases, the sedimentation rate is dramatically increased by the presence of salt in the fluid.

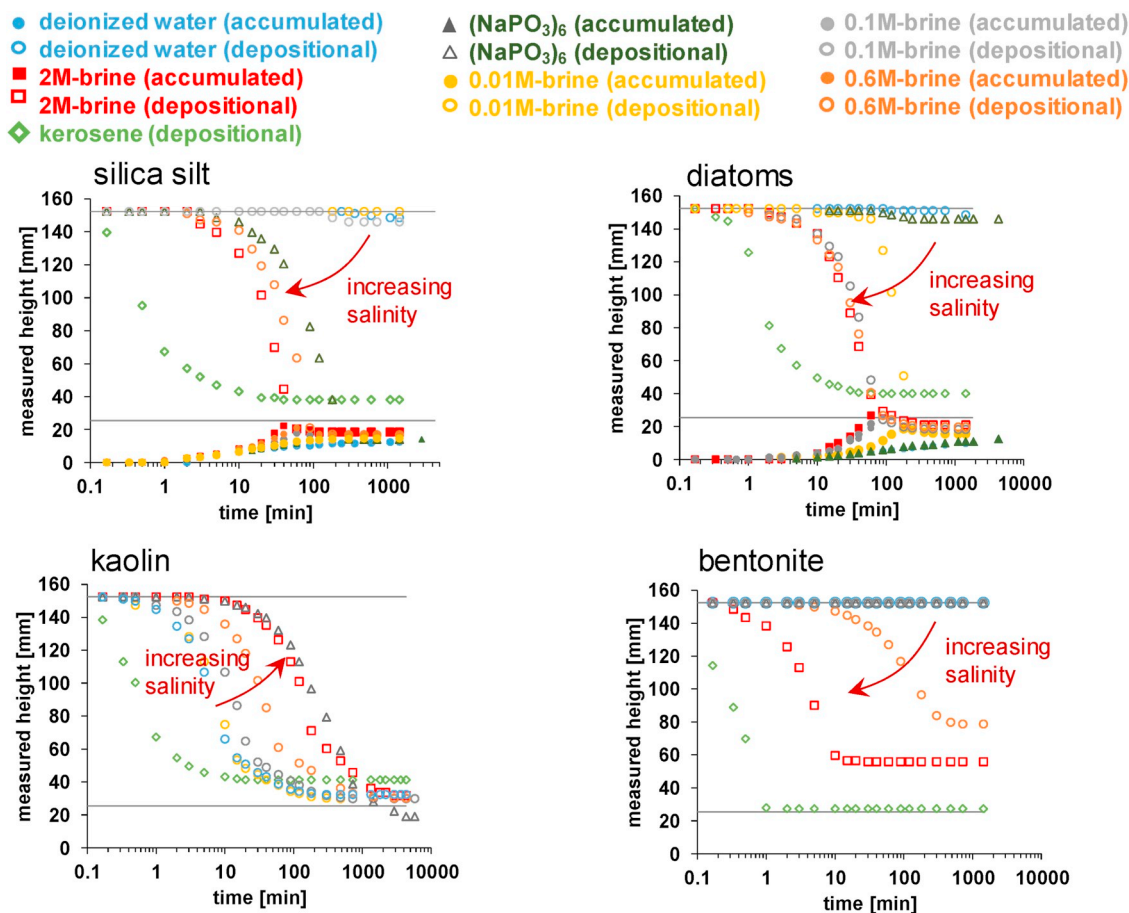


Fig. 8. Sedimentation patterns of endmember fines: silica silt, diatoms, kaolin and bentonite (for physical properties and detailed descriptions of sedimentations refer to Jang et al., 2018a, b). The UBGH2 results most closely follow the sedimentation behavior of diatoms.

sediment height as a loose fabric. Because the accumulated interface heights in DWS and 2M-brine are so close to 25.4 mm, we infer that any additional interparticle interaction effects due to the dilution from 2M-brine to DWS, such as swelling, are minimal even though the samples contain clay minerals. Comparing the results of UBGH2 samples to endmember tests in Fig. 8, all UBGH2 results follow the diatom pattern of rapidly increasing sedimentation rates with even small increases in salt concentration solutions. Clay minerals identified in the XRD spectra are also part of the turbid supernatant, but it is the diatoms that appear to control the sedimentation behavior of fines in these UBGH2 samples.

4.3. Micromodel test: clogging at pore throats

Micromodel tests with mixtures of UBGH2 samples began with the configuration having the lowest potential for clogging: the smallest sediment concentration of 0.1% (weight ratio of sediment to liquid) in the micromodel with the largest pore throats (100 μm). Following the approach of Cao et al. (2019), the plan was to increase the sediment concentration and decrease pore throat size until clogging was observed. However, only one set of tests was run because clogging occurred in that first, lowest clogging potential situation for both the deionized water and the 2M brine pore fluids. Fig. 9 shows images from the single-phase and multi-phase pore water fluid flow testing for UBGH2-6B-18H-3. The left image in Fig. 9a shows the clogged condition in the micromodel after the single-phase injection of 0.1 wt% sediment mixed with deionized water. After this single-fluid-phase injection from the left side of the micromodel, fluid was withdrawn from the left while CO₂ gas was introduced from the right. The right image shows the clogged condition after the subsequent CO₂ injection test.

Across all three samples, the number of clogs at pore throats was

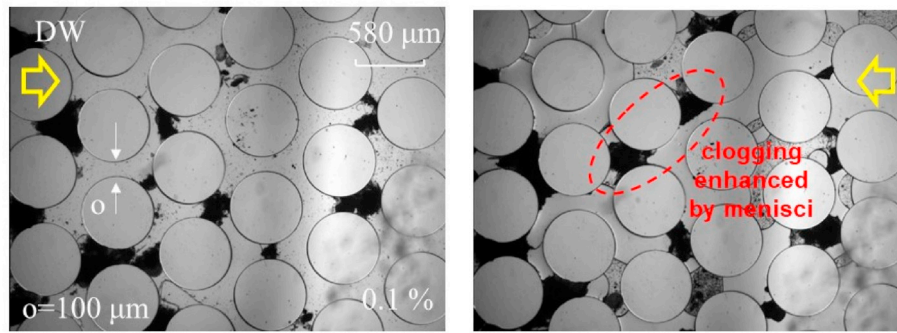
slightly more frequent in deionized water (25% of pore throats clogged) than in brine (17% clogging) within the viewing area of the micromodel chip, but this distinction essentially vanished after CO₂ gas invasion (27% and 25% clogging in DW and brine, respectively). These results agree with the Cao et al. (2018, 2019) data for pure diatoms, which also indicated clogging occurred with the lowest measured sediment concentration (0.1 wt%) and the absence of a strong dependence of clogging on pore-fluid chemistry.

The concentration of fines by a mobile gas/water interface is highlighted in the right panels of Fig. 9a and b, where residual water accumulating at pore throats has dark, high fines-concentration menisci. The gas-liquid interfaces also collected and concentrated fine grains within the areas bounded by those interfaces. As shown in Fig. 9a and b (right panels), this meniscus-based concentration of fines can create new pore-throat clogs (dashed red ovals). Enhanced fines concentration and clogging due to a mobile interface has been observed previously (Muecke, 1979; Jung et al., 2012, 2018a; 2018b Han et al., 2018; Cao et al., 2019). As observed for diatoms by Cao et al. (2019), the enhanced clogging due to the mobile meniscus is not strongly dependent on pore-water chemistry.

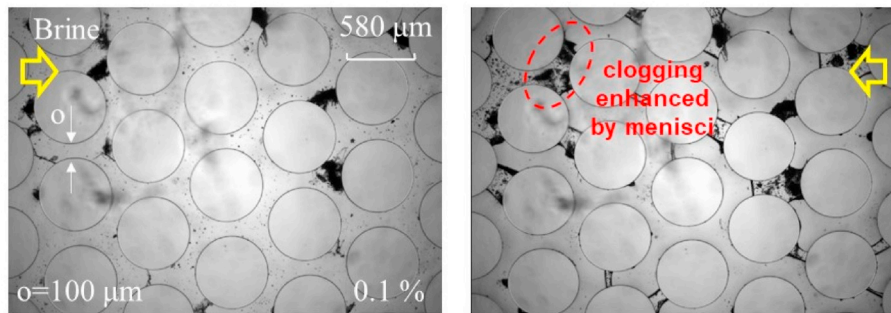
The presence of diatoms can accentuate clogging through purely physical mechanisms as well as chemistry-based clustering. As shown in Fig. 9c, diatoms in UBGH2 sediments can be large enough to clog via sieving (e.g., Fig. 1b), and the irregular shapes of diatom shards facilitates the shards becoming ensnared and blocking larger pore throats.

5. Implications: freshening effects on fines in fluid flow during gas production

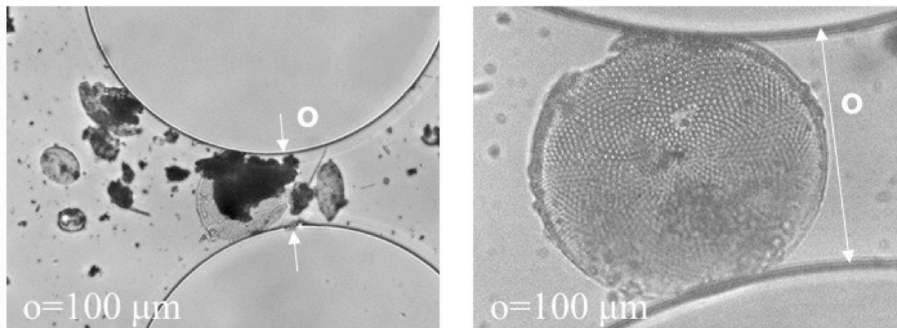
As seen in the SEM imagery (Figs. 5 and 6) and results from the



(a)



(b)



(c)

Fig. 9. 2D micromodel images of clogging with 0.1 wt% UBGH2-18H-3 sediment in the injected pore fluid. Circles are the solid “grains,” and the pore-throats (o) are 100 μm across. Dark clusters represent clusters of fines. (a) Images are for single-phase deionized water (left) and two-phase CO₂ injection (right). The injection direction is given by the yellow arrow in each figure. (b) Single-phase 2M-brine (left) and CO₂ injection (right). (c) Examples of clogging by a diatom via the mechanical process of sieving. (For interpretation of the references to colour in this figure legend, the reader is referred to the Web version of this article.)

sedimentation and 2D micromodel testing, diatoms are abundant in the UBGH2 fines and play a central role in the behavior of the UBGH2 sediment samples as salinity changes. Entrained diatoms are sensitive to the presence of saline water, but once the salinity exceeds ~1–8% of the assumed seawater salinity, 0.6M, the behavior of diatoms is only weakly dependent on salinity changes. Following the approach of Mohan et al. (1993), the critical salinity threshold below which fines detachment become significant, is set at 8% of the assumed seawater salinity for these specific UBGH2 specimens. When sandy gas hydrate-bearing sediment with the ~80% gas hydrate saturation (S_h) inferred for UBGH2-6 by Lee and Collett (2013) dissociates, the diluted pore water salinity (c_{dil}) becomes 25% of the original salinity (c_o). This calculation assumes the dissociated water volume is ~79% of the initial

methane hydrate volume, based on a methane hydrate stoichiometry of CH₄·5.75H₂O and a methane hydrate density of 910 kg/m³ (Sloan and Koh, 2007):

$$c_{dil} = \frac{c_o(1 - S_h)}{(1 - S_h) + 0.79S_h} \quad (1)$$

For freshening to dilute the pore water enough to affect detachment of fines in the UBGH2 samples, based on the sedimentation test results, the hydrate saturation would have to exceed ~93% of the available pore space if all dissociated water remained in the pores.

Regarding detachment or resuspension of diatoms, a more important consideration than pore-water freshening is localized fluid flow. Preferential dissociation of gas hydrate along the interfaces between gas

hydrate-bearing sands and the fine-grained interbeds leads to preferential fluid flow toward the production well along these interfaces (Myshakin et al., 2019; Uchida et al., 2019). The drag force on particles is proportional to the particle size at low Re (laminar flow) in Stokes' law, and resistance to the seepage force and erodibility decreases with decreasing specific gravity of the particles (Lambe and Whitman, 1969; Grabowski et al., 2011). Plasticity, or cohesion between particles, can increase the particle's resistance to erosion or resuspension, so clay minerals tend to be more difficult to resuspend than silty particles (Roberts et al., 1998; Grabowski et al., 2011). In comparison to clay minerals, diatoms and diatom shards can be relatively large (e.g. Fig. 9c), are non-plastic, have low specific gravity, and are thus relatively easily entrained into the fluid flow along interfaces between the fine-grained interbeds and sandy hydrate-bearing sediment in the gas hydrate intervals observed in the Ulleung Basin. Based on the observed clogging even at only 0.1 wt% sediment, combined with the relative ease of resuspending diatoms and diatom shards, clogging by clusters of shards of diatoms is expected once fines migration occurs. As shown in Fig. 9c, even 100 μm pore throats, close to the maximum pore throat size in the sandy hydrate-bearing sediment in Ulleung Basin, are susceptible to clogging via sieving by individual diatoms entrained in the pore-water flow.

Although diatoms appear to dominate the behavior of the UBGH2 fines tested here, XRD results highlight the presence of muscovite and illite (Table 2), both of which are more easily resuspended as the pore water salinity decreases (Mohan et al., 1993; Civan, 2016). In particular, the XRD results and changes in LL_{DW} and $LL_{2M,corr}$ for UBGH2-6B-18H-3 (Table 1) suggest the UBGH2-6 interbeds contain enough salinity-sensitive clay minerals (primarily illite) to be responsive to salinity changes during gas hydrate dissociation. The interbed mud layers at UBGH2-6 would increase their rate of clay-mineral detachment during pore-water freshening, accentuating the potential for clogging beyond the clogging due to diatoms and diatom shards.

The mobile gas/water interface generated during gas hydrate dissociation further enhances clogging for all tested samples regardless of pore-water chemistry. The increased clogging potential due to the mobile meniscus' capacity to collect and concentrate fines is difficult to quantify for the UBGH2 samples because the UBGH2 fines, and the diatoms in particular are already at the upper limit for detection using the approach of Cao et al. (2019). The high clogging potential observed in these specimens indicates there will be a high likelihood of clogging even if only small concentrations of fines are resuspended (~ 0.1 wt% of the pore fluid). For radial collection of fluids by a central production well, fines are concentrated as they move inward toward the well (Valdes and Santamarina, 2007), making it increasingly likely that the low threshold for clogging by fines can be reached.

6. Conclusions

The detachment and clogging potential of fines located along interfaces between thin, gas hydrate-bearing sands and fine-grained interbeds in two Ulleung Basin gas hydrate reservoirs has been found to be high and will increase as gas hydrate dissociation progresses during production. These sediments are likely to be mobilized during production because interfaces between coarse- and finer-grained intervals are significant regions for gas hydrate dissociation and elevated fluid/gas flow.

In this study, selected mud interbed samples from UBGH2-2B-15C, UBGH2-6B-18H-3 and UBGH2-6C-6P were tested to assess the extent to which resuspension of fines from reservoir interfaces with these interbeds could contribute to clogging during production activities. All three samples were found to contain high enough concentrations of diatoms for those diatoms to control the physical properties and clogging behavior of those fine-grained interbeds. The concentration of diatoms in the UBGH2 sediment has two important consequences for clogging during production:

- Diatoms and diatom shards, which have low specific gravities and are relatively easy to resuspend relative to more cohesive fines, easily block even the 100 μm pore throats that represent the largest anticipated pore throats in the UBGH2 gas hydrate-bearing sands. Clogging occurs even at the lowest tested concentration of fines in the pore water (0.1 wt%), and individual diatoms (~ 100 μm in diameter) are capable of clogging pore throats via sieving.
- Diatoms are not highly sensitive to pore-water chemistry changes, meaning that for the $\sim 80\%$ peak gas hydrate saturations inferred for these UBGH2 sites, the diatom resuspension and clogging potential will remain fairly constant as the pore water freshens during production. Should the local gas hydrate saturation exceed $\sim 93\%$, however, the diatoms would become increasingly easy to resuspend in the production flow.

Though diatoms dominated the sedimentation and clogging behavior at the laboratory scale, XRD results show other types of fines such as muscovite and illite are significant components of the UBGH2 fines studied here. Muscovite and illite fines are more sensitive to pore water salinity changes than are diatoms, and pore-water freshening increases both the ease of resuspension and clogging potential of these platy fines. As production proceeds, these fines are anticipated to contribute to the clogging potential of the diatoms and diatom shards. The clogging potential of these sediments will also be accentuated once gas hydrate dissociation generates mobile gas-water interfaces.

CRediT authorship contribution statement

Junbong Jang: Conceptualization, Methodology, Investigation, Formal analysis, Writing - original draft. **Shuang C. Cao:** Conceptualization, Methodology, Investigation, Writing - review & editing. **Laura A. Stern:** Conceptualization, Methodology, Investigation, Writing - review & editing. **William F. Waite:** Conceptualization, Methodology, Investigation, Writing - review & editing. **Jongwon Jung:** Conceptualization, Methodology, Investigation, Supervision, Resources, Writing - review & editing. **Joo Yong Lee:** Conceptualization, Methodology, Investigation, Writing - review & editing.

Declaration of competing interest

The authors declare that they have no known competing financial interests or personal relationships that could have appeared to influence the work reported in this paper.

Acknowledgements

This work was supported by the U. S. Department of Energy (DOE) through interagency agreements with the U.S. Geological Survey (DE-FE00-23495 and DE-FE00-26166) and a grant awarded to Louisiana State University (DE-FE00-28966); and by the Ministry of Trade, Industry, and Energy (MOTIE) through the Project "Gas Hydrate Exploration and Production Study (20-1143)" under the management of the Gas Hydrate Research and Development Organization (GHDO) of Korea and the Korea Institute of Geoscience and Mineral Resources (KIGAM), and by the Ministry of Education through the National Research Foundation of Korea (NRF) to the Basic Science Research Program (2017R1D1A3B03031369). Sedimentation data is available on-line at <https://doi.org/10.5066/P9UJOYVR>. The authors wish to thank C. Ruppel and two anonymous reviewers for their constructive comments on this manuscript. Any use of trade, firm or product name is for descriptive purposes only and does not imply endorsement by the U. S. Government.

Appendix A. Supplementary data

Supplementary data to this article can be found online at <https://doi.org/10.1016/j.marpetgeo.2020.104244>.

References

- Anderson, B., Boswell, R., Collett, T.S., Farrell, H., Ohtsuki, S., White, M., Zyrianova, M., 2014. Review of the findings of the Ignik Sikumi CO₂-CH₄ gas hydrate exchange field trial. In: Proceedings of the 8th International Conference on Gas Hydrates. United States: China Geological Survey, Beijing, China.
- Andreola, F., Castellini, E., Manfredini, T., Romagnoli, M., 2004. The role of sodium hexametaphosphate in the dissolution process of kaolinite and kaolin. *J. Eur. Ceram. Soc.* 24 (7), 2113–2124. [https://doi.org/10.1016/S0955-2219\(03\)00366-2](https://doi.org/10.1016/S0955-2219(03)00366-2).
- Andrews, J.T., Eberl, D.D., Kristjansdottir, G.B., 2006. An exploratory method to detect tephra from quantitative XRD scans: examples from Iceland and east Greenland marine sediments. *Holocene* 16 (8), 1035–1042. <https://doi.org/10.1177/0959683606069384>.
- ASTM, 2005. Standard Test Methods for Liquid Limit, Plastic Limit, and Plasticity Index of Soils. ASTM International, West Conshohocken, PA ASTM D4318.
- ASTM, 2007. Standard Test Method for Particle-Size Analysis of Soils. ASTM D422. ASTM, West Conshohocken, PA.
- ASTM, 2011. Standard Practice for Classification of Soils for Engineering Purposes (Unified Soil Classification System). ASTM D2487. ASTM, West Conshohocken, PA.
- Bahk, J.J., Kim, G.Y., Chun, J.H., Kim, J.H., Lee, J.Y., Ryu, B.J., Lee, J.H., Son, B.K., Collett, T.S., 2013. Characterization of gas hydrate reservoirs by integration of core and log data in the Ulleung Basin, East Sea. *Mar. Pet. Geol.* 47, 30–42. <https://doi.org/10.1016/j.marpetgeo.2013.05.007>.
- Bigno, Y., Oyenein, M.B., Peden, J.M., 1994. Investigation of pore-blocking mechanism in gravel packs in the management and control of fines migration. In: SPE-27342-MS. SPE Formation Damage Control Symposium, Lafayette, Louisiana, 9–10 Feb, <https://doi.org/10.2118/27342-MS>.
- Boswell, R., Collett, T.S., 2011. Current perspectives on gas hydrate resources. *Energy Environ. Sci.* 4 (4), 1206–1215. <https://doi.org/10.1039/c0ee00203h>.
- Boswell, R., Marsteller, S., Okinaka, N., Wakatsuki, M., Collett, T.S., Hunter, R., Walsh, T., Minge, D., Itter, D., Crumley, S., 2019a. Viable long-term gas hydrate testing site confirmed on the Alaska North Slope. *Fire in the Ice: Dep. Energy Office Fossil Energy Natl. Energy Technol. Lab.* 19 (1), 1–5.
- Boswell, R., Myshakin, E., Moridis, G., Konno, Y., Collett, T.S., Reagan, M., Ajayi, T., Seol, Y., 2019b. India National Gas Hydrate Program Expedition 02 summary of scientific results: numerical simulation of reservoir response to depressurization. *Mar. Pet. Geol.* 108, 154–166. <https://doi.org/10.1016/j.marpetgeo.2018.09.026>.
- Boswell, R., Yamamoto, K., Lee, S.R., Collett, T., Kumar, P., Dallimore, S., 2014. Chapter 8 - methane hydrates. In: Letcher, T.M. (Ed.), *Future Energy*. Elsevier, Boston.
- British Standard Institute BSI, 1990. *Methods of Test for Soils for Civil Engineering Purpose*. BS 1377. BSI (British Standards Institution), London.
- Cao, S.C., Jang, J., Jung, J., Waite, W.F., Collett, T.S., Kumar, P., 2018. 2D Micromodel Studies of Pore-Throat Clogging by Pure Fine-grained Sediments and Natural Sediments from NGHP-02, Offshore India. U. S. Geological Survey data release <https://doi.org/10.5066/P9PZ5M7E>.
- Cao, S.C., Jang, J., Jung, J., Waite, W.F., Collett, T.S., Kumar, P., 2019. 2D micromodel study of clogging behavior of fine-grained particles associated with gas hydrate production in NGHP-02 gas hydrate reservoir sediments. *Mar. Pet. Geol.* 108, 714–730. <https://doi.org/10.1016/j.marpetgeo.2018.09.010>.
- Chough, S.K., Barg, E., 1987. Tectonic history of Ulleung Basin margin, East Sea (sea of Japan). *Geology* 15 (1), 45–48. [https://doi.org/10.1130/0091-7613\(1987\)15<45:THOUBM>2.0.CO;2](https://doi.org/10.1130/0091-7613(1987)15<45:THOUBM>2.0.CO;2).
- Civan, F., 2016. *Reservoir Formation Damage*. Elsevier, Massachusetts.
- Collett, T.S., Johnson, A.H., Knapp, C.C., Boswell, R., 2009. Natural gas hydrates: a review. In: Collett, T.S., Johnson, A.H., Knapp, C.C., Boswell, R. (Eds.), *Natural Gas Hydrates - Energy Resource Potential and Associated Geologic Hazards*, vol. 89. AAPG Memoir, pp. 146–219 AAPG Memoir 89.
- Dallimore, S.R., Collett, T.S., 2005. Summary and implications of the Mallik 2002 gas hydrate production research well program. In: Dallimore, S.R., Collett, T.S. (Eds.), *Scientific Results from the Mallik 2002 Gas Hydrate Production Research Well Program*, Mackenzie Delta, Northwest Territories, Canada. Bulletin, vol. 585. Geological Survey of Canada, pp. 1–36.
- Dallimore, S.R., Yamamoto, K., Wright, J.F., Bellefleur, G., 2012. Proof of concept for gas hydrate production using the depressurization technique, as established by the JOGMEC/NRCAN/Aurora Mallik 2007–2008 Gas Hydrate Production Research Well Program. In: Dallimore, S.R., Yamamoto, K., Wright, J.F., Bellefleur, G. (Eds.), *Scientific Results from the JOGMEC/NRCAN/Aurora Mallik 2007–2008 Gas Hydrate Production Research Well Program*, Mackenzie Delta, Northwest Territories, Canada. Bulletin 601. Geological Survey of Canada, pp. 1–15.
- Dressaire, E., Sauret, A., 2017. Clogging of microfluidic systems. *Soft Matter* 13, 37–48. <https://doi.org/10.1039/c6sm01879c>.
- Fagel, N., Boski, T., Likhoshway, L., Oberhaensli, H., 2003. Late quaternary clay mineral record in central lake baikal (abercanization ridge, siberia). *Palaeogeogr. Palaeoclimatol. Palaeoecol.* 193 (1), 159–179. [https://doi.org/10.1016/S0031-0182\(02\)00633-8](https://doi.org/10.1016/S0031-0182(02)00633-8).
- Grabowski, R.C., Droppo, I.G., Wharton, G., 2011. Erodibility of cohesive sediment: the importance of sediment properties. *Earth Sci. Rev.* 105, 101–120. <https://doi.org/10.1016/j.earscirev.2011.01.008>.
- Han, G., Kwon, T.H., Lee, J.Y., Kneafsey, A.J., 2018. Depressurization-induced fines migration in sediments containing methane hydrate: X-ray computed tomography imaging experiments. *J. Geophys. Res. Solid Earth* 123 (4), 2539–2558. <https://doi.org/10.1002/2017jb014988>.
- Hancock, S., Boswell, R., Collett, T., 2019. Development of deepwater natural gas hydrates. In: *Offshore Technology Conference*, Houston, Texas, May 6–9, OTC-29374-MS. <https://www.doi.org/10.4043/29374-MS>.
- Handa, Y.P., 1986. Calorimetric determinations of the compositions, enthalpies of dissociation, and heat-capacities in the range 85 to 270-K for clathrate hydrates of xenon and krypton. *J. Chem. Thermodyn.* 18 (9), 891–902. [https://doi.org/10.1016/0021-9614\(86\)90124-2](https://doi.org/10.1016/0021-9614(86)90124-2).
- Ingle, J.C., 1992. Subsidence of the Japan Sea: stratigraphic evidence from ODP sites and onshore sections. In: Tamaki, K., Suyehiro, K., Allan, J., McWilliams, M. (Eds.), *Proceedings of Ocean Drilling Program, Scientific Results*. 127/128 Part 2, pp. 1197–1218 (College Station, TX).
- Ivanov, I.B., Kralchevsky, P.A., Nikolov, A.D., 1986. Film and line tension effects on the attachment of particles to an interface. I. Conditions for mechanical equilibrium of fluid and solid particles at a fluid interface. *J. Colloid Interface Sci.* 112 (1), 97–107. [https://doi.org/10.1016/0021-9797\(86\)90072-X](https://doi.org/10.1016/0021-9797(86)90072-X).
- Jang, J., Cao, S.C., Stern, L.A., Jung, J., Waite, W.F., 2018a. Impact of pore fluid chemistry on fine-grained sediment fabric and compressibility. *J. Geophys. Res. Solid Earth* 123 (7), 5495–5514. <https://doi.org/10.1029/2018jb015872>.
- Jang, J., Cao, S.C., Stern, L.A., Waite, W.F., Jung, J., 2018b. Effect of Pore Fluid Chemistry on the Sedimentation and Compression Behavior of Pure, Endmember Fines. U.S. Geological Survey data release <https://doi.org/10.5066/F77M076K>.
- Jang, J., Santamarina, J.C., 2016. Fines classification based on sensitivity to pore-fluid chemistry. *J. Geotech. Geoenviron. Eng.* 142 (4), 06015018. [https://doi.org/10.1061/\(ASCE\)GT.1943-5606.0001420](https://doi.org/10.1061/(ASCE)GT.1943-5606.0001420). Artn 06015018.
- Jang, J., Waite, W.F., Stern, L., Collett, T.S., Kumar, P., 2019. Physical property characteristics of gas hydrate-bearing reservoir and associated seal sediments collected during NGHP-02 in the Krishna-Godavari Basin, in the offshore of India. *Mar. Pet. Geol.* 108, 249–271. <https://doi.org/10.1016/j.marpetgeo.2018.09.027>.
- Jung, J., Cao, S.C., Shin, Y.-H., Al-Raoush, R.I., Alshibli, K., Choi, J.-W., 2018a. A microfluidic pore model to study the migration of fine particles in single-phase and multi-phase flows in porous media. *Microsyst. Technol.* 24, 1071–1080.
- Jung, J., Kang, H., Cao, S.C., Al-Raoush, R.I., Alshibli, K., Lee, J.Y., 2018b. Effects of fine-grained particles' migration and clogging in porous media on gas production from hydrate-bearing sediments. *Geofluids* 2019, 1–11.
- Jung, J.W., Jang, J., Santamarina, J.C., Tsouris, C., Phelps, T.J., Rawn, C.J., 2012. Gas production from hydrate-bearing sediments: the role of fine particles. *Energy Fuels* 26 (1), 480–487. <https://doi.org/10.1021/ef101651b>.
- Khilari, K.C., Fogler, H.S., 1998. *Migrations of Fines in Porous Media*. Springer, Netherlands.
- Kim, A.R., Kim, J.T., Cho, G.C., Lee, Y.J., 2018. Methane production from marine gas hydrate deposits in Korea: thermal-hydraulic-mechanical simulation on production wellbore stability. *J. Geophys. Res.: Solid Earth* 123, 9555–9569. <https://doi.org/10.1029/2018JB015875>.
- Kim, G.Y., Yi, B.Y., Yoo, D.G., Ryu, B.J., Riedel, M., 2011. Evidence of gas hydrate from downhole logging data in the Ulleung Basin, East Sea. *Mar. Pet. Geol.* 28, 1979–1985. <https://doi.org/10.1016/j.marpetgeo.2011.01.011>.
- Kim, J.-H., Torres, M.E., Hong, W.-L., Choi, J., Michael, R., Bahk, J.-J., Kim, S.-H., 2013. Pore fluid chemistry from the second gas hydrate drilling expedition in the Ulleung Basin (UBGH2): source, mechanisms and consequences of fluid freshening in the central part of the Ulleung Basin, East Sea. *Mar. Pet. Geol.* 47, 99–112. <https://doi.org/10.1016/j.marpetgeo.2012.12.011>.
- Kurihara, M., Funatsu, K., Ouchi, H., Sato, A., Yasuda, M., Narita, H., Masuda, Y., Dallimore, S.R., Wright, F., 2011. Analysis of 2007/2008 JOGMEC/NRCAN/AURORA Mallik gas hydrate production test through numerical simulation. In: *The 7th International Conference on Gas Hydrates (ICGH 2011)*, Edinburgh, Scotland, United Kingdom.
- Kwon, T.H., Lee, K.R., Cho, G.C., Lee, J.Y., 2011. Geotechnical properties of deep oceanic sediments recovered from the hydrate occurrence regions in the Ulleung Basin, East Sea, offshore Korea. *Mar. Pet. Geol.* 28 (10), 1870–1883. <https://doi.org/10.1016/j.marpetgeo.2011.02.003>.
- Lagaly, G., 1989. Principles of flow of kaolin and bentonite dispersions. *Appl. Clay Sci.* 4 (2), 105–123. <https://doi.org/10.1063/1.447541>.
- Lambe, T.W., Whitman, R.V., 1969. *Soil Mechanics*. John Wiley & Sons, New York.
- Lee, J.Y., Kim, G.Y., Kang, N.K., Yi, B.Y., Jung, J.W., Im, J.H., Son, B.K., Bahk, J.J., Chun, J.H., Ryu, B.J., 2013a. Physical properties of sediments from the Ulleung Basin, East Sea: results from second Ulleung Basin gas hydrate drilling expedition, East Sea (Korea). *Mar. Pet. Geol.* 47, 43–55.
- Lee, J.S., Lee, J.Y., Kim, Y.M., Lee, C., 2013b. Stress-dependent and strength properties of gas hydrate-bearing marine sediments from the Ulleung Basin, East Sea, Korea. *Mar. Pet. Geol.* 47, 66–76. <https://doi.org/10.1016/j.marpetgeo.2013.04.006>.
- Lee, G.H., Suk, B.-C., 1998. Latest neogene-quaternary seismic stratigraphy of the Ulleung Basin, East Sea (sea of Japan). *Mar. Geol.* 146, 205–224. [https://doi.org/10.1016/S0025-3227\(97\)00123-0](https://doi.org/10.1016/S0025-3227(97)00123-0).
- Lee, M.W., Collett, T.S., 2013. Scale-dependent gas hydrate saturation estimates in sand reservoirs in the Ulleung Basin, East Sea of Korea. *Mar. Pet. Geol.* 47, 168–181. <https://doi.org/10.1016/j.marpetgeo.2012.09.003>.
- Li, J.-f., Ye, J.-l., Qin, X.-w., Hai-jun, Q., Wu, N.-y., Lu, H.-l., Xie, W.-w., Lu, J.-a., Fei, P., Xu, Z.-q., Lu, C., Kuang, Z.-g., Wei, J.-g., Liang, Q.-y., Lu, H.-f., Kou, B.-b., 2018. The first offshore natural gas hydrate production test in South China Sea. *China Geology* 1 (1), 5–16. <https://doi.org/10.31035/cg2018003>.
- McDonald, J.C., Whitesides, G.M., 2002. Poly(dimethylsiloxane) as a material for fabricating microfluidic devices. *Acc. Chem. Res.* 35 (7), 491–499.
- Mitchell, J.K., Soga, K., 2005. *Fundamentals of Soil Behavior*. John Wiley & Sons, Inc.,

- New Jersey.
- Mohan, K.K., Vaidya, R.N., Reed, M.G., Fogler, H.S., 1993. Water sensitivity of sandstones containing swelling and non-swelling clays. *Colloid. Surf. Physicochem. Eng. Asp.* 73, 237–254. [https://doi.org/10.1016/0927-7757\(93\)80019-B](https://doi.org/10.1016/0927-7757(93)80019-B).
- Moridis, G.J., Kim, J., Reagan, M.T., Kim, S.J., 2013. Feasibility of gas production from a gas hydrate accumulation at the UBGH2-6 site of the Ulleung basin in the Korean East Sea. *J. Pet. Sci. Eng.* 108, 180–210. <https://doi.org/10.1016/j.petrol.2013.03.002>.
- Moridis, G.J., Reagan, M.T., Queiruga, A.F., Kim, S.J., 2019. System response to gas production from a heterogeneous hydrate accumulation at the UBGH2-6 site of the Ulleung basin in the Korean East Sea. *J. Pet. Sci. Eng.* 178, 655–665. <https://doi.org/10.1016/j.petrol.2019.03.058>.
- Muecke, T.W., 1979. Formation fines and factors controlling their movement in porous-media. *J. Pet. Technol.* 31 (2), 144–150. <https://doi.org/10.2118/7007-Pa>.
- Myshakin, E., Lin, J.S., Uchida, S., Seol, Y., Collett, T., Boswell, R., 2019. Numerical simulation of depressurization-induced gas production from an interbedded turbidite hydrate-bearing sedimentary section in the offshore of India: site NGHP-02-16 (Area-B). *Mar. Pet. Geol.* 108, 619–638. <https://doi.org/10.1016/j.marpetgeo.2018.10.047>.
- Oyama, H., Abe, S., Yoshida, T., Sato, T., Nagao, J., Tenma, N., Narita, H., 2016. Experimental study of mud erosion at the interface of an artificial sand-mud alternate layer. *J. Nat. Gas Sci. Eng.* 34, 1106–1114. <https://doi.org/10.1016/j.jngse.2016.07.067>.
- Oyenein, M.B., Peden, J.M., Hosseini, A., Ren, G., 1995. Factors to consider in the effective management and control of fines migration in high permeability sands. In: SPE-30112-MS. European Formation Damage Conference, Hague, Netherlands, 15–16 May, <https://doi.org/10.2118/30112-MS>.
- Palomino, A.M., Santamarina, J.C., 2005. Fabric map for kaolinite: effects of pH and ionic concentration on behavior. *Clay Clay Miner.* 53 (3), 209–222. <https://doi.org/10.1346/CCMN.2005.0530302>.
- Pierre, A.C., Ma, K., 1999. DLVO theory and clay aggregate architectures formed with AlCl₃. *J. Eur. Ceram. Soc.* 19 (8), 1615–1622. [https://doi.org/10.1016/S0955-2219\(98\)00264-7](https://doi.org/10.1016/S0955-2219(98)00264-7).
- Poppe, L.J., Paskevich, V.F., Hathaway, J.C., Blackwood, D.S., 2001. A laboratory manual for X-ray powder diffraction. In: *A Laboratory Manual for X-Ray Powder Diffraction* U.S. Geological Survey Open-File Report 01-041.
- Roberts, J., Jepsen, R., Gotthard, D., Lick, W., 1998. Effects of particle size and bulk density on erosion of quartz particles. *J. Hydraul. Eng. ASCE* 124 (12), 1261–1267. [https://doi.org/10.1061/\(ASCE\)0733-9429\(1998\)124:12\(1261\)](https://doi.org/10.1061/(ASCE)0733-9429(1998)124:12(1261)).
- Ryu, B.J., Collett, T.S., Riedel, M., Kim, G.Y., Chun, J.H., Bahk, J.J., Lee, J.Y., Kim, J.H., Yoo, D.G., 2013. Scientific results of the second gas hydrate drilling expedition in the Ulleung Basin (UBGH2). *Mar. Pet. Geol.* 47, 1–20. <https://doi.org/10.1016/j.marpetgeo.2013.07.007>.
- Ryu, B.J., Riedel, M., Kim, J.H., Hyndman, R.D., Lee, Y.J., Chung, B.H., Kim, I.S., 2009. Gas hydrates in the western deep-water Ulleung Basin, East Sea of Korea. *Mar. Pet. Geol.* 26 (8), 1483–1498. <https://doi.org/10.1016/j.marpetgeo.2009.02.004>.
- Santamarina, J.C., Dai, S., Terzariol, M., Jang, J., Waite, W.F., Winters, W.J., Nagao, J., Yoneda, J., Konno, Y., Fujii, T., Suzuki, K., 2015. Hydro-bio-geomechanical properties of hydrate-bearing sediments from Nankai Trough. *Mar. Pet. Geol.* 66, 434–450. <https://doi.org/10.1016/j.marpetgeo.2015.02.033>.
- Santamarina, J.C., Klein, K.A., Fam, M.A., 2001. *Soils and Waves*. John Wiley & Sons, New York.
- Santamarina, J.C., Klein, K.A., Wang, Y.H., Prencke, E., 2002. Specific surface: determination and relevance. *Can. Geotech. J.* 39, 233–241. <https://doi.org/10.1139/t01-077>.
- Shiwakoti, D.R., Tanaka, H., Tanaka, M., Locat, J., 2002. Influences of diatom microfossils on engineering properties of soils. *Soils Found.* 42 (3), 1–17. <https://doi.org/10.3208/sandf.42.3.1>.
- Sloan, E.D., Koh, C.A., 2007. *Clathrate Hydrates of Natural Gases*. CRC Press, Taylor & Francis Group, LLC, New York.
- Sogami, I., Ise, N., 1984. On the electrostatic interaction in macroionic solutions. *J. Chem. Phys.* 81 (12), 6320–6332. <https://doi.org/10.1063/1.447541>.
- Tanaka, H., Locat, J., 1999. A microstructural investigation of Osaka Bay clay: the impact of microfossils on its mechanical behaviour. *Can. Geotech. J.* 36, 493–508. <https://doi.org/10.1139/t99-009>.
- Torres, M.E., Trehu, A.M., Cespedes, N., Kastner, M., Wortmann, U.G., Kim, J.H., Long, P., Malinverno, A., Pohlman, J.W., Riedel, M., Collett, T., 2008. Methane hydrate formation in turbidite sediments of northern Cascadia. IODP Expedition 311. *Earth Planet. Sci. Lett.* 271 (1–4), 170–180. <https://doi.org/10.1016/j.epsl.2008.03.061>.
- Uchida, S., Lin, J.S., Seol, Y., Collett, T., Boswell, R., 2019. Numerical simulation of sand production in interbedded hydrate-bearing sediments at Site NGHP-02-16. *Mar. Pet. Geol.* 108, 639–647. <https://doi.org/10.1016/j.marpetgeo.2018.10.046>.
- Valdes, J.R., Santamarina, J.C., 2007. Particle transport in a nonuniform flow field: retardation and clogging. *Appl. Phys. Lett.* 90 (24), 244101. <https://doi.org/10.1063/1.2748850>.
- Waite, W.F., Jang, J., Collett, T.S., Kumar, P., 2019. Downhole physical properties-based description of a gas hydrate petroleum system in NGHP-02 Area C: a channel, levee, fan complex in the Krishna-Godavari Basin offshore eastern India. *Mar. Pet. Geol.* 108, 272–295. <https://doi.org/10.1016/j.marpetgeo.2018.05.021>.
- Wroth, C.P., Wood, D.M., 1978. The correlation of index properties with some basic engineering properties of soils. *Can. Geotech. J.* 15 (2), 137–145. <https://doi.org/10.1139/t78-014>.
- Yamamoto, K., Kanno, T., Wang, X.X., Tamaki, M., Fujii, T., Chee, S.S., Wang, X.W., Pimenov, V., Shako, V., 2017. Thermal responses of a gas hydrate-bearing sediment to a depressurization operation. *RSC Adv.* 7 (10), 5554–5577. <https://doi.org/10.1039/c6ra26487e>.
- Yamamoto, K., Suzuki, K., Wang, X., Matsunaga, T., Nishioka, I., Nakatsuka, Y., Yoneda, J., 2019. The second offshore production test of methane hydrates in the Eastern Nankai Trough and site characterization efforts. *Fire in the Ice: Dep. Energy Office Fossil Energy Natl. Energy Technol. Lab.* 19 (1), 9–15.
- Yamamoto, K., Terao, Y., Fujii, T., Ikawa, T., Seki, M., Matsuzawa, M., 2014. Operational overview of the first offshore production test of methane hydrates in the Eastern Nankai Trough. In: *Offshore Technology Conference, OTC 25243*.
- Yoo, D.G., Kang, N.K., Yi, B.Y., Kim, G.Y., Ryu, B.J., Lee, K., Lee, G.H., Riedel, M., 2013. Occurrence and seismic characteristics of gas hydrate in the Ulleung Basin, East Sea. *Mar. Pet. Geol.* 47, 236–246. <https://doi.org/10.1016/j.marpetgeo.2013.07.001>.
- Yu, T., Guan, G.Q., Abudula, A., 2019. Production performance and numerical investigation of the 2017 offshore methane hydrate production test in the Nankai Trough of Japan. *Appl. Energy* 251. <https://doi.org/10.1016/j.apenergy.2019.113338>.